Supporting Information

Solé-Domènech et al. 10.1073/pnas.1719808115

SI Effect of N- and C-Terminal Cleavages on FEPs

The FEPs for θ_{14} and γ_{14} were discussed in the main text (Fig. 4). Similar to the FEPs for H14, cleavages after residues K16 or F20 induce additional minima for the θ FEPs of most N-terminal peptides within the first β-sheet domain (Fig. S6*A*). Cleavages after K16 and F20 also induce shallower FEPs, especially along the γ angles, for resulting peptides within the second and third β-sheet domains, compared with the intact peptide. This effect, however, is modest (Fig. S6*B*). This is in agreement with MD results, which indicated that cleavages after residues K16 and F20 facilitated release of the resulting N-terminal fragments from the β-sheet template, with a more modest effect on the release of the resulting C-terminal fragments (Fig. 4 *A* and *B*).

Cleavages near the C terminus (after residues G33, L34, M35, V36, G38, and V40) do not induce large variations in conformational flexibility for the resulting N-terminal peptides compared with the intact peptide. However, these cleavages do induce increased flexibility for some C-terminal peptides. Cleavages near the C terminus generally induce shallower FEPs along γ angles for some peptides within the second and third β-sheet domains (Fig. S6*B*). This is in agreement with MD calculations, which indicated that cleavages along the C terminus do not have a significant effect on the release of N-terminal fragments from the fibril template, but they do favor the release of C-terminal fragments (Fig. 4 *C*–*H*).

SI Materials and Methods

For all described procedures buffers and hardware were either autoclaved or washed with NaOH 0.5 M for 15 min to eliminate any traces of contaminants and proteases.

proTPP1 Activation. Recombinant proTPP1 was expressed in CHO cells and purified by column chromatography as previously described (1). Aliquots (10 mg/mL) were stored in artificial cerebrospinal fluid. For enzyme activation, proTPP1 was diluted 1–10 in 150 mM NaCl with 100 mM sodium formate, pH 3.5, for 2–3 h at 37 °C. After activation, the enzyme preparation was aliquoted in vials (20 μL each) and snap-frozen in liquid nitrogen followed by storage at –80 °C.

TPP1 Activity Assay. Before incubation with AβCy3 nanofibrils the activity of activated TPP1 was estimated by incubation of 100 nM enzyme with 200 μM Ala-Ala-Phe-7-amido-4-methylcoumarin (A3401; Sigma-Aldrich) diluted in 150 mM NaCl with 100 mM sodium acetate at pH 3.0 or pH 4.5. The hydrolysis of Ala-Ala-Phe-7-amido-4methylcoumarin by TPP1 releases fluorescent 7-aminocoumarin, which can be monitored in a plate reader. For kinetic assays, plates were placed in a 37 °C sample chamber of a SpectraMax M2 plate reader (Molecular Devices). The plates were read from the bottom using 351-nm excitation and 450-nm emission wavelengths. Plates were read at 5-min intervals for 60 min and mixed for 5 s before and within each reading.

Labeling of Synthetic $A\beta_{1–42}$ with Cy3. Synthetic $A\beta_{1–42}$ (AS-60883; Anaspec) was solubilized at 1 mg/mL in cold 50 mM sodium tetraborate, pH 9.3, briefly vortexed and sonicated for 1 min, and vortexed again. The solution was kept on ice during handling. After solubilization, the contents of the solution were added to a vial of Cy3 monoreactive succinimidyl ester dye (PA23001; GE Healthcare). The mixture was incubated under constant rotation for 30–60 min at room temperature, protected from light, and thereafter dialyzed in cold 50 mM pH 9.3 sodium tetraborate using a 3.5-kDa dialysis cassette (66330; Thermo Scientific) with four buffer changes over 1 d. After dialysis, AβCy3 was removed from the dialysis cassette and stored at 4 °C in low-adhesion tubes (1415-2600; USA Scientific). AβCy3 labeling efficiency and Cy3 concentration were determined by measuring the absorbance of the centrifuged supernatant at 552 nm (ε_{Cy3} is 150,000 $M^{-1}\cdot cm^{-1}$). The preparation was centrifuged for 1 h at 4 °C (1,320,000 × *g*·min) and the resulting pellet was discarded. The preparation was used within a month.

Preparation of AβCy3 Fibrils for TPP1 Digestion. One milligram of $A\beta_{1–42}$ was solubilized at 1 mg/mL in 1 mL of 50 mM sodium tetraborate, pH 9.3. After solubilization, $A\beta_{1–42}$ was immediately diluted 1–10 in pH 7.4 PBS buffer (22.1 μM). Cy3-labeled $A\beta_{1–42}$ was added to the dilution so that the ratio of AβCy3:Aβ was 0.06. The fibrillation mixture was prepared in sealed, 4-mL polycarbonate ultracentrifuge tubes (362305; Beckman Coulter) and incubated for 24–48 h at 37 °C under constant rotation. After incubation, fibrillar AβCy3 was isolated by two ultracentrifugation steps at 4 °C (1 h each, 9×10^6 *g*·min). After the first centrifugation, the supernatants were carefully discarded, and the pellets were washed in PBS pH 7.4 buffer. After the last ultracentrifugation step, the pellets were resuspended in pH 3.0 or 4.5 buffers for TPP1 digestion, and the protease inhibitors PMSF (1 mM), EDTA (5 mM), pepstatin-A (10 μM), and E-64 (250 μM) were added. The resulting mixtures were sonicated using a probe sonicator (Misonix, 6 × 20 s, <20 W power). During sonication, the polycarbonate tubes containing the fibrillar preparations remained in ice, and 1-min pauses between each 20-s sonication intervals were used to prevent overheating. After sonication, the Cy3 concentration of the fibrillar preparation was determined by absorbance at 552 nm.

Negative-Stain Electron Microscopy Imaging of Sonicated Fibrillar Mixtures. Fibrillar, purified Aβ pellets were resuspended in PBS buffer by gentle pipetting. A drop (10–20 μL) of resuspended fibrils was placed onto a coated copper grid (FCF400-Cu; Electron Microscopy Sciences) and allowed to sit for 1 min, followed by labeling with uranyl acetate. The preparation was imaged using a JEOL JEM 1400 transmission electron microscope, with an acceleration voltage of 120 kV. Images were acquired using a Veletta CCD camera.

Digestions of AβCy3 Nanofibrils with TPP1. AβCy3 nanofibrils resuspended in 150 mM NaCl, 100 mM sodium acetate buffers (adjusted to pH 3.0 or pH 4.5) were aliquoted into Falcon tubes and allowed to warm up at 37 °C in a water bath for 15 min. TPP1 was added to a final concentration of 200 nM in aliquots containing either AβCy3 nanofibrils alone or nanofibrils plus 600 μM enzyme inhibitor. As inhibitor of TPP1 enzymatic activity we used AAF-CMK. A tube containing AβCy3 nanofibrils without enzyme or inhibitor was included in the experiment as control for baseline Cy3 fluorescence. Mixtures were incubated at 37 °C for 15, 30 and 60 min. Zero-time points were sampled before adding TPP1 to the mixtures. After each time point, 500 μL of reaction mixture for each condition were collected into a low-adhesion Eppendorf tube and diluted 1:1 in 50 mM sodium tetraborate, pH 9.3. AAF-CMK was immediately added to the diluted crude reaction mixture to a final concentration of 300 μM. The diluted mixture was briefly vortexed and ultracentrifuged for 1 h at 4 °C (3×10^7 *g*·min). Next, 100 μL supernatant were collected per time point and condition and plated in a 384-well plate (20 μL per well, two wells per condition) for Cy3 fluorescence

measurements. Twenty microliters of the supernatant from each time point were also collected and snap-frozen in liquid nitrogen for MS analysis.

Cy3 Fluorescence Measurements. Cy3 standards (0–100 nM) were prepared by dilution of Cy3 succinimidyl ester (PA23001; GE Healthcare), initially solubilized in 50 mM pH 9.3 sodium tetraborate buffer and then diluted in PBS. Twenty-microliter samples and standards were plated into a 384-well plate (two wells per condition) and Cy3 fluorescence was measured for each well using a Leica EPI fluorescence microscope (10× objective, Cy3 filter). Fluorescence measurements were carried out 150 μm above the bottom of the well. The Cy3 concentration in the supernatants was determined, and the percentage of digestion for each time point was calculated relative to the initial Cy3 concentration of the fibrillar preparations before digestion.

MS of Digestion Mixtures. Each sample (19 μL) was acidified with 1 μL of 10% formic acid and 2 μL analyzed by nano LC-MS/MS using a Dionex Ultimate 3000 RLSCnano System interfaced with Velos LTQ Orbitrap (Thermo Fisher). Samples were loaded onto a self-packed 100-μm × 2-cm trap (Magic C18AQ, 5 μm 200 Å; Michrom Bioresources, Inc.) and washed with buffer A (0.2% formic acid) for 5 min with a flow rate of 10 μL/min. The trap was brought in-line with the analytical column (Magic C18AQ, 3 μm 200 Å, 75 μm × 50 cm) and peptides fractionated at 300 nL/min using a segmented linear gradient 4–15% B (0.2% formic acid in acetonitrile) in 5 min, 15–50% B in 25 min. MS data were acquired using a data-dependent acquisition procedure. Each cycle consisted of a full MS1 scan acquired with resolution of 60,000 on the orbitrap mass analyzer and MS/MS of the 20 most intense ions (collision-induced dissociation with relative collision energy of 35%, scanned in the ion trap mass analyzer) using a repeat count of 2 and a dynamic exclusion duration of 40 s. Peptides were initially identified using a local implementation of the global proteome machine (2), to search precursor/fragment ion peak lists against custom databases containing human A beta 1–42 and human TPP1 sequences, allowing cleavage at all residues. Precursor ion peak areas from Aβ peptides were quantified using XCalibur software (Thermo Scientific).

Molecular Modeling. $A\beta_{1-42}$ fibrils were built based on the model by Xiao et al. (3). The model provides coordinates for residues 11–42 only, as residues 1–10 were disordered and could not be resolved. A fibril template, consisting of a fibril containing six chains, was simulated (Fig. 3*A*). As shown in previous work (4), to give the template the stability of a multichain fibril, distance restraints were applied to the backbones of all residues in the two chains at the core (depicted by white arrows in Fig. 3*A*). Because the K28–A42 salt bridge cannot be reproduced with the UNRES force field, the salt bridge was simulated by restraining the distance between the virtual peptide groups of K28 and A42 in all six chains (Fig. 2*B*). These restraints do not directly affect the binding between chains because the different chains in a fibril are held together by intermolecular hydrogen bonds (Fig. 3*B*). Nine different systems were simulated: a six-chain fibril template without cleavage and a six-chain fibril template where the chains at the end of the template were cleaved after residues K16, F20, G33, L34, M35, V36, G38, and A40 (Fig. 3*C*). Therefore, when simulating the cleavage by TPP1, two cleavages were introduced, one at each end of the fibril (top and bottom in Fig. 3*A*). Cleavages were not mixed (i.e., the cleavage site at the top and bottom was the same for each simulated system). The cleavage after residue Y10 was not simulated because the first 10 aa of the $A\beta_{1-42}$ sequence are unstructured, and the cleavage is unlikely to alter β-sheet stability.

Force Field for MD Simulations. MD simulations were carried out using the UNRES force field (5–8) (Fig. S5) with the Berendsen thermostat. For each cleavage site (e.g., after residues K16 and F20), 120 canonical independent trajectories were generated. Each trajectory was 7×10^6 steps long, which is equivalent to 14 ns (9, 10), generating an accumulated time of ∼1.7 μs. The last 7 ns of simulation on each trajectory were used for the analysis.

1. Lin L, Lobel P (2001) Production and characterization of recombinant human CLN2 protein for enzyme-replacement therapy in late infantile neuronal ceroid lipofuscinosis. *Biochem J* 357:49–55.
2. Beavis RC (2006) Using the global proteome machine for protein identification. *Methods Mol Biol* 328:217–228.
3. Xiao Y, et al. (2015) Aβ(1-42) fibril structure illuminates self-recognition and replication of amyloid in Alzheimer's disease. *Nat Struct Mol Biol* 22:499–505.
4. Rojas A, Liwo A, Browne D, Scheraga HA (2010) Mechanism of fiber assembly: Treatment of Aβ peptide aggregation with a coarse-grained united-residue force field. *J Mol Biol* 404:537–552.
5. Liwo A, Czaplewski C, Pillardy J, Scheraga HA (2001) Cumulant-based expressions for the multibody terms for the correlation between local and electrostatic interactions in the united-residue force field. *J Chem Phys* 115:2323–2347.
6. Rojas AV, Liwo A, Scheraga HA (2007) Molecular dynamics with the united-residue force field: Ab initio folding simulations of multichain proteins. *J Phys Chem B* 111:293–309.
7. Liwo A, et al. (2007) Modification and optimization of the united-residue (UNRES) potential energy function for canonical simulations. I. Temperature dependence of the effective energy function and tests of the optimization method with single training proteins. *J Phys Chem B* 111:260–285.
8. He Y, Xiao Y, Liwo A, Scheraga HA (2009) Exploring the parameter space of the coarse-grained UNRES force field by random search: Selecting a transferable medium-resolution force field. *J Comput Chem* 30:2127–2135.
9. Khalili M, Liwo A, Rakowski F, Grochowski P, Scheraga HA (2005) Molecular dynamics with the united-residue model of polypeptide chains. I. Lagrange equations of motion and tests of numerical stability in the microcanonical mode. *J Phys Chem B* 109: 13785–13797.
10. Khalili M, Liwo A, Jagielska A, Scheraga HA (2005) Molecular dynamics with the united-residue model of polypeptide chains. II. Langevin and Berendsen-bath dynamics and tests on model alpha-helical systems. *J Phys Chem B* 109:13798–13810.

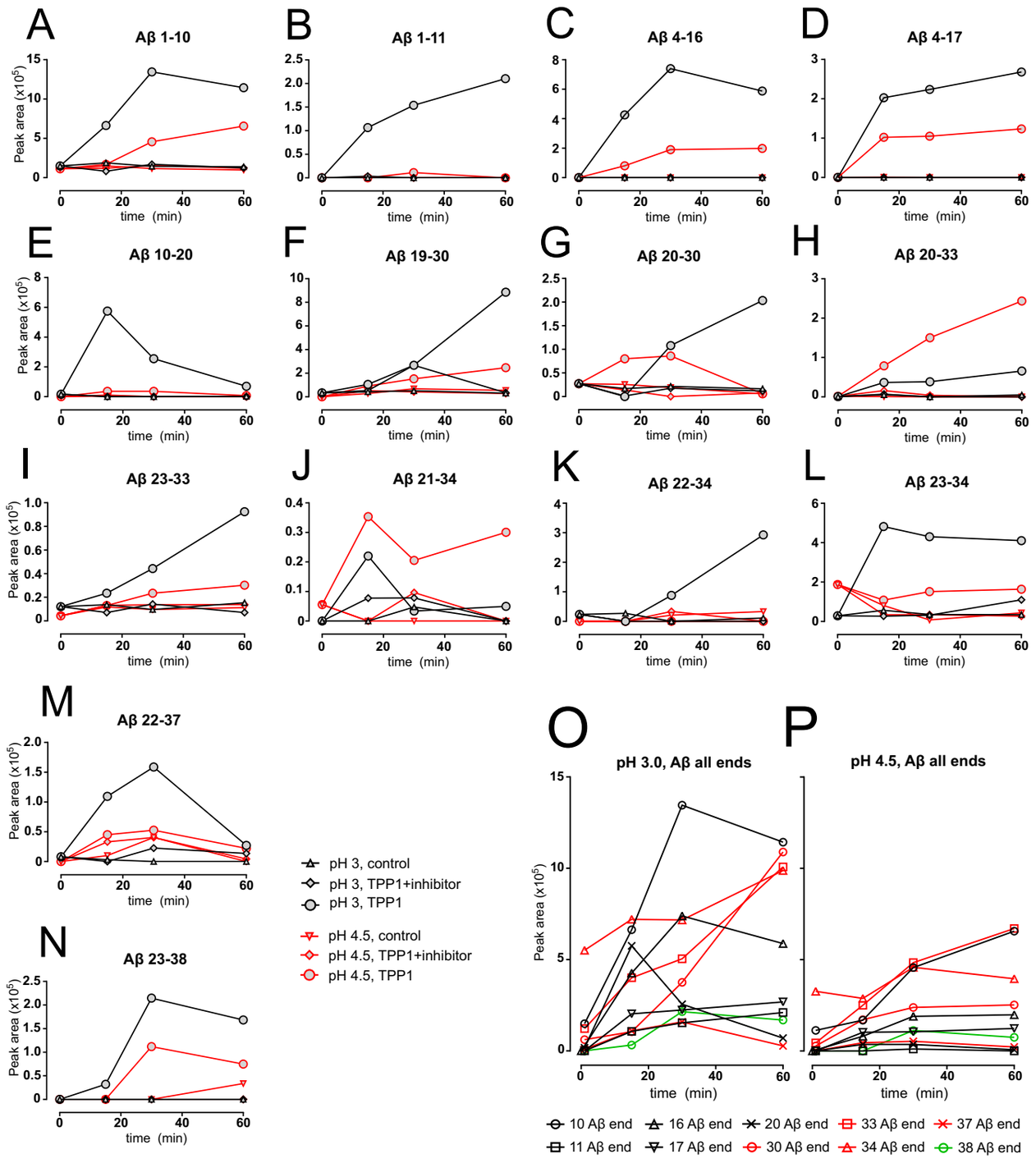

Fig. S1. Individual N- and C-terminal peptide fragments detected by MS analysis of monomeric Aβ digested with TPP1. *A*–*N* show peak areas as function of digestion times. Circle-dotted black and red lines refer to digestions conducted in pH 3.0 and pH 4.5 buffers in presence of TPP1, whereas all other (black or red) lines indicate digestions either in absence of TPP1 or in presence of the enzyme coincubated with H-AAF-CMK inhibitor. The various conditions are identified in the legend at the bottom of the figure. Multiple N-terminal peptide fragments were detected by MS; (*A*) peak area for peptide fragment 1–10, indicative of cleavage after residue E10. (*B*) Peak area for peptide fragment 1–11 indicative of cleavages after residue Y11. (*C*) Peak area for fragment 4–16, indicative of cleavage after K16. (*D*) Peak area for fragment 4–17 indicative of cleavage after L17. (*E*) Peak areas for fragment 10–20, indicative of cleavage after F20. A number of C-terminal fragments were also observed; (*F* and *G*) peak area for fragments 19–30 and 20–30, respectively, indicative of cleavage after A30, (*H* and *I*) peak areas for fragments 20–33 and 23–33, respectively, indicative of cleavage after G33. (*J*–*L*) Peak area for fragments 21–34, 22–34, and 23–34, respectively, indicative of cleavage after L34. (*M*) Peak area for fragment 22–37, indicative of cleavage after residue G37. (*N*) Peak area for fragment 23–38, indicative of cleavage after G38. (*O* and *P*) Sum of peak areas for peptide fragments ending in a specific residue as function of digestion time and pH. Each peptide ending is indicated in the legend below the panel. Peak areas for fragments 19–30 and 20–30 have been added and denominated 30 Aβ end, indicative of cleavage after residue A30. Peak areas for fragments 20–33 and 23–33 have also been added and denominated 33 Aβ end, indicative of cleavage after residue G33. Peak areas for fragments 21–34, 22–34 and 23–34 have been integrated and presented as 34 Aβ end, representative of cleavage after residue L34.

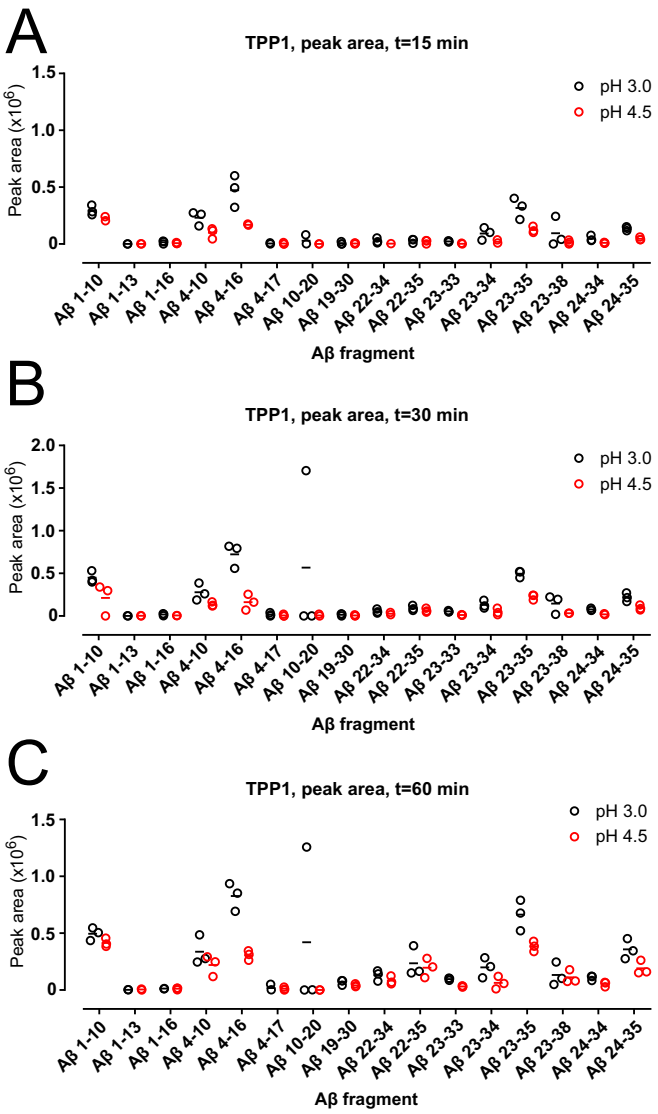

Fig. S2. Peak areas for all peptides detected by MS analysis of AβCy3 nanofibrils, digested with TPP1. Three peak area values are presented for each peptide, corresponding to three experimental replicates. *A*–*C* show peak areas obtained after 15, 30, and 60 min digestion, respectively. Incubations in pH 3.0 and 4.5 buffers are indicated by black and red circles, respectively.

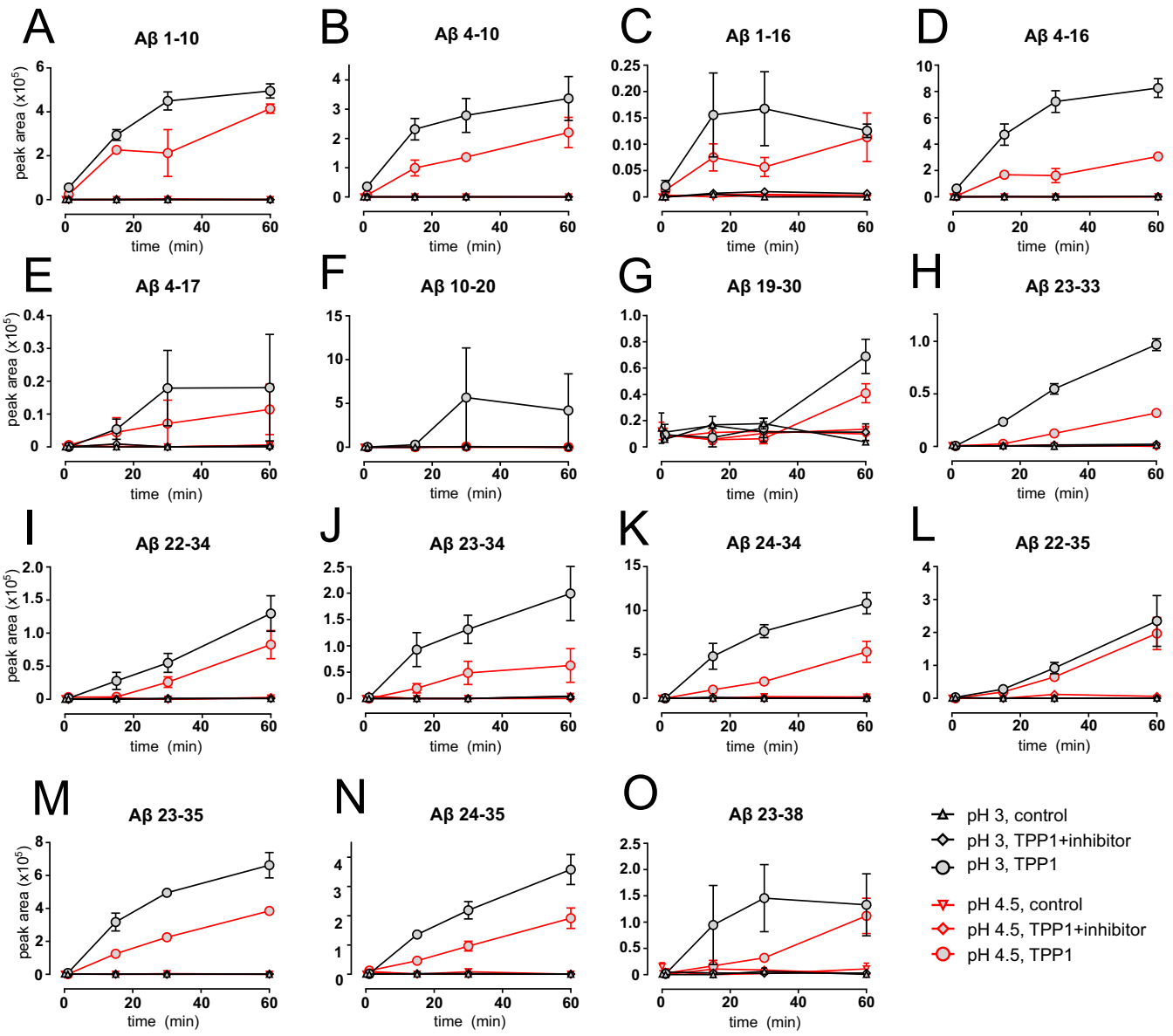

Fig. S3. Individual peptides detected by MS analysis of AβCy3 nanofibrils digested with TPP1. A number of N-terminal peptides were detected. (*A* and *B*) Peak areas for detected peptides 1–10 and 4–10, respectively, indicative of cleavage after residue E10. (*C* and *D*) Peak areas for peptides 1–16 and 4–16, respectively, indicative of cleavage after amino acid K16. (*E*) Peak area for peptide fragment 4–17, indicative of cleavage after residue L17. Moreover, a number of C-terminal peptides were also detected. (*F*) Peak area for peptide 10–20, indicative of cleavage after residue F20. (*G*) Peak area for peptide 19–30, indicative of cleavage after residue A30. (*H*) Peak area for peptide 23–33, representative of cleavage after residue G33, (*I*–*K*) peak areas for peptides 22–34, 23–34, and 24–34, respectively, representative of cleavages after residue L34. (*L*–*N*) Peak areas for peptides 22–35, 23–35, and 24–35, respectively, representative of cleavage after residue M35; (*O*) peak area for peptide fragment 23–38, representative of cleavage after residue G38. All peptide abundances increase with increasing acidity, in agreement with the data on Cy3 release as function of time and pH presented in Fig. 2*B*, and clearly differ from peptide formation in absence of TPP1 or when coincubated with AAF-CMK inhibitor. The various experimental conditions are indicated in the legend located to the lower right corner of the figure. The average of three experiments is presented. Bars indicate standard error of the mean.

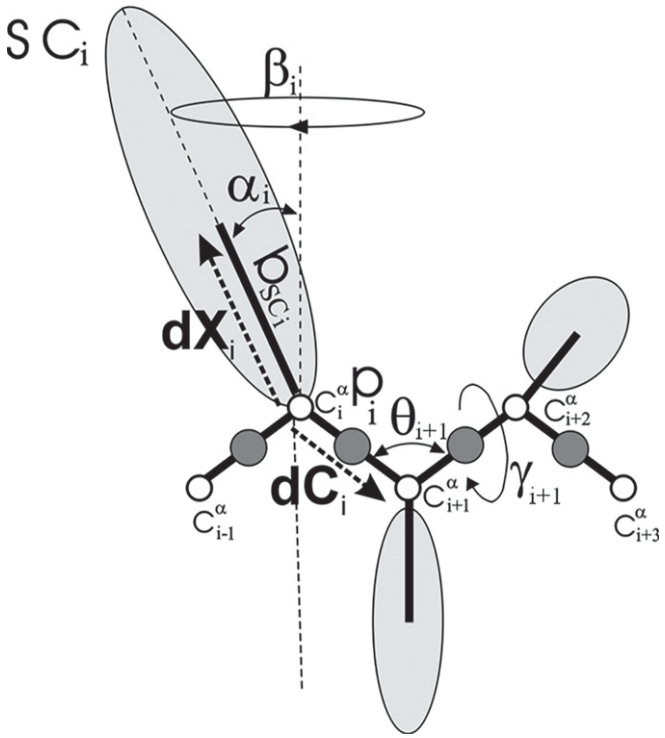

Fig. S4. The UNRES model of polypeptide chains. The interaction sites are peptide-bond centers (p) and side-chain ellipsoids of different sizes (SC) attached to the corresponding α-carbons with different "bond lengths," b_{SC}. The α-carbon atoms are represented by small open circles. The equilibrium distance of the C^α ••• C^α virtual bonds is taken as 3.8 Å, which corresponds to planar *trans* peptide groups. The geometry of the chain can be described either by the virtual-bond vectors $\mathbf{dC}_i$ ($C^\alpha_i \ldots C^\alpha_{i+1}$), $i = 1, 2, \ldots, N - 1$ and $\mathbf{dX}_i$ ($C^\alpha_i \ldots SC_i$), $i = 2, 3, \ldots, N - 1$ (represented by thick dashed arrows, where N is the number of residues) or in terms of virtual-bond lengths, backbone virtual-bond angles θ_i, $i = 2, 3, \ldots, N - 1$, backbone virtual-bond-dihedral angles γ_i, $i = 2, 3, \ldots, N - 2$, and the angles α_i and β_i, $i = 2, 3, \ldots, N - 1$ that describe the location of a side chain with respect to the coordinate frame defined by C^α_{i-1}, C^α_i, and C^α_{i+1}.

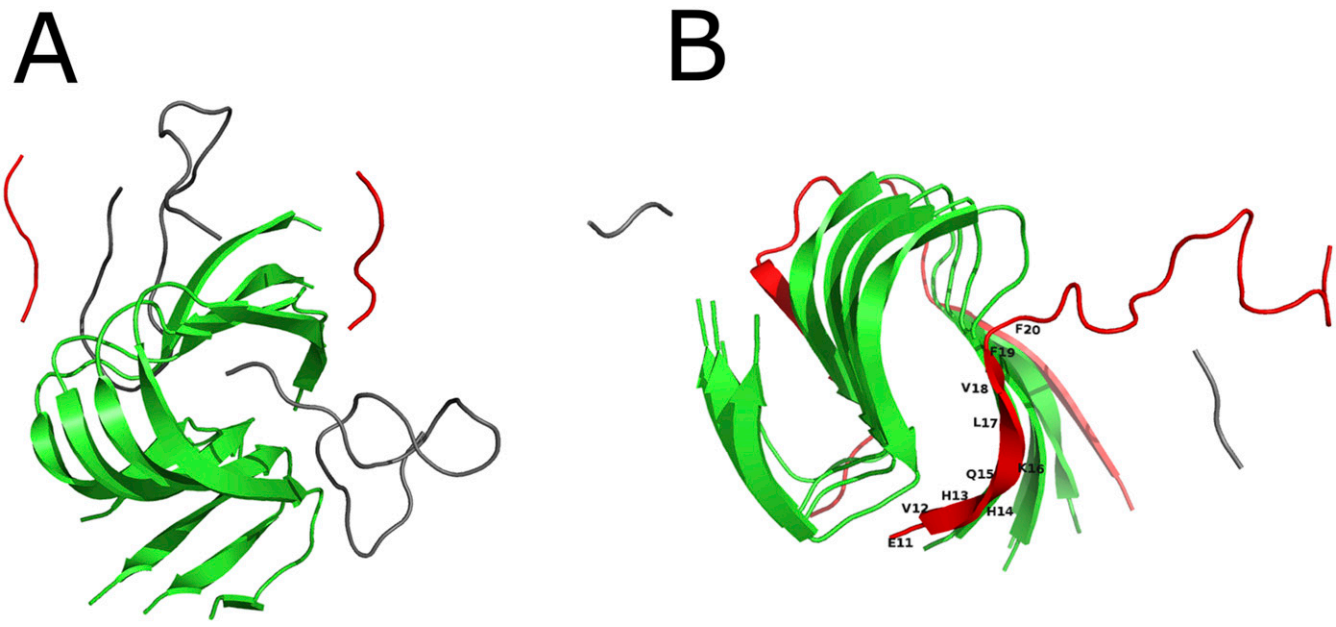

Fig. S5. Representative snapshots from simulations of cleavages after K16 and F21. (*A*) Cleavage after residue K16. The template is shown in green. The fragments resulting from the cleavage, $A\beta_{11-16}$ and $A\beta_{17-42}$, are shown in red and gray, respectively. Both fragments, from either end of the template, have been released. (*B*) Cleavage after residue G38. The fragments resulting from the cleavage, $A\beta_{11-38}$ and $A\beta_{39-42}$, are shown in red and gray, respectively. The C-terminal fragments from either end of the template have been released. The N-terminal fragment at the front of the figure shows how residues 21–42 are no longer bound to the template, but the chain fragment remains attached to it through hydrogen bonds formed along residues 11–20.

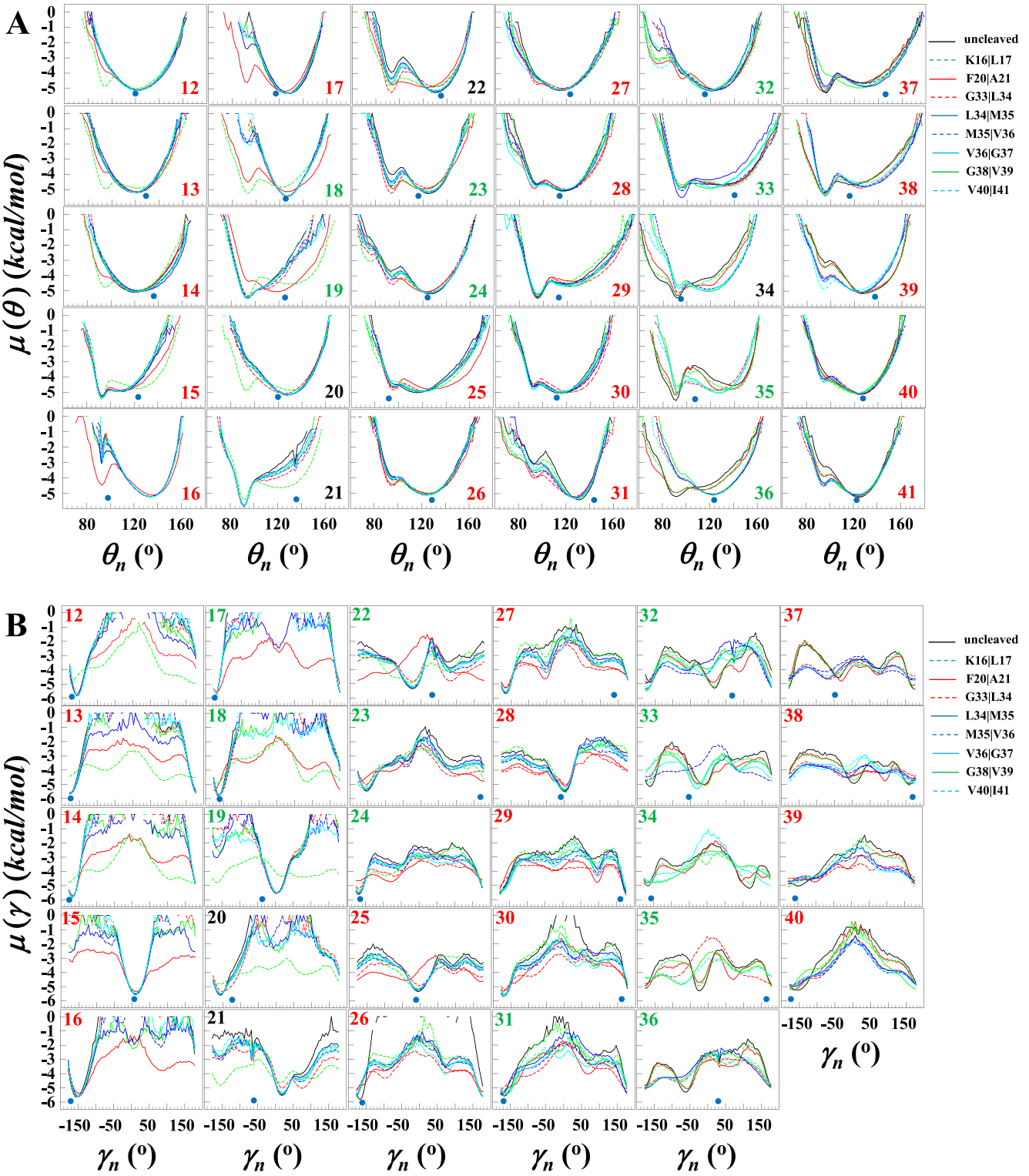

Fig. S6. FEPs, μ(θ) (*A*) and μ(γ) (*B*), along the θ and γ angles for eight peptides cleaved at specific sites and for one intact peptide. The peptides for which the FEPs were calculated are indicated in the legend below *A* and *B*. The black numbers pertain to FEPs along the θ and γ angles which include only residues of the loop; the red numbers pertain to FEPs along the θ and γ angles which include only residues of β-strands; the green numbers pertain to FEPs along θ and γ angles which include the residues from both loop and β-strands. The NMR-derived structural data (blue circles at the bottom of each panel) are computed from the first model of the PDB ID code 2MXU (3).